Two-dimensional Fourier spectroscopy applied to electron-phonon correlations in quantum well intersubband systems

Thi Uyen-Khanh Dang,[*] Carsten Weber,[†] Sebastian Eiser,[‡] Andreas Knorr, and Marten Richter
Institut für Theoretische Physik, Nichtlineare Optik und Quantenelektronik, Technische Universität Berlin, Hardenbergstrasse 36, EW 7-1, 10623 Berlin, Germany
(Received 28 February 2012; revised manuscript received 17 August 2012; published 9 October 2012)

Two-dimensional photon echo spectroscopy allows one to track relaxation and correlation processes in optically excited nanostructures. We analyze such spectra for intersubband transitions in an n-doped $GaAs/Al_{0.35}Ga_{0.65}As$ single quantum well. Focusing on electron-longitudinal optical phonon interaction in a non-Markovian treatment, the carrier dynamics in the conduction subbands are investigated in the low density regime. Our results provide detailed information about the temporal evolution of electron-phonon correlations in the two-dimensional frequency spectrum.

DOI: 10.1103/PhysRevB.86.155306 PACS number(s): 42.50.Md, 63.20.kd, 78.67.De, 78.47.J−

Semiconductor quantum well (QW) devices based on the dynamics in the intersubband (ISB) regime are the foundation for various optoelectronic applications.[1–3] In order to gain a deeper understanding of the underlying microscopic processes that drive the performance of such devices, ISB systems have been widely investigated experimentally as well as theoretically.[4–10] There, clear signatures of electron-electron (el-el) and electron-phonon (el-ph) scattering can be observed in the linear excitation regime as line shape broadening and satellite peaks in absorption spectra.[11–13] In the nonlinear regime, a large variety of coherent spectroscopy schemes, for example, pump-probe or four wave mixing experiments, have been used to investigate complex many-body interactions in semiconductor nanostructures.[14] In standard transient experiments the ultrafast dynamics are observed as a change of transmission or absorption,[15–17] yielding indirect information about the electronic population. Another, more complex access to the investigation of many-body interactions was developed in nuclear magnetic resonance (NMR),[18] where multiple quantum transitions (i.e., pathways), whose analysis provide a more detailed information on correlated induced excitation frequencies, are selectively detected in two-dimensional (2D) Fourier transform spectroscopy.[19,20] The extraction of these pathways requires a multipulse setup, where in the experiment the time delays between the different pulses is varied. The signal is then Fourier transformed with respect to the time delays, leading to a 2D frequency spectrum. The development of ultrashort laser pulses up to the visible spectrum[21,22] allowed for this method to be applied to a wide range of biological systems and semiconductor nanostructures,[23–27] giving access to detailed structural information of the investigated system.[28–32] For example, 2D spectroscopy has been performed experimentally on coupled ISB QWs by Kuehn *et al.* recently, detecting strong polaronic signatures in the nonlinear response.[33] To separate different blocks of quantum pathways, common experiments use a noncollinear setup (incoming pulses propagate in different directions),[34] where different quantum pathways are emitted in different directions of the wave vector. Another approach is to use a collinear setup, where the superposed quantum pathways can be separated by the so-called phase cycling (PC) technique.[35–37] Here the phases of the incoming time-ordered pulses are varied for each repetition of the experiment. When combining the outcoming response signals, multiple quantum pathways can be extracted. If no Fourier transform is applied, PC can also be used to extract certain quantum pathways from simulations in the time domain.[38]

In this paper we present a microscopic 2D photon echo signal study, applied to the ISB dynamics of an n-doped $GaAs/Al_{0.35}Ga_{0.65}As$ single QW and discuss its benefits for detecting many-body interactions in ISB systems. In the simulation a collinear three pulse setup excites the sample and a PC protocol will be used to extract the photon echo signal.[39] To correctly model the 2D Fourier transform experiments we will address the following topics in the article: After introducing the theoretical background of the coherent 2D spectroscopy, the PC method will be described. Next, the investigated QW model based on a microscopic Heisenberg equation of motion approach is derived. Finally, the results are presented in Sec. IV, where an in-depth interpretation of the 2D frequency spectrum reveals the signatures of electronic correlations by means of a direct mapping of excitation and response in the 2D frequency spectrum. It will be shown that the spectra give detailed information about the quantum kinetics and relaxation processes of electrons due to their interaction with longitudinal optical (LO) phonons.

I. COHERENT 2D SPECTROSCOPY

At first it is necessary to investigate the dependence of the material response on the incoming optical pulses. Here we assume an electromagnetic field consisting of three collinear, temporally separated pulses:[40]

$$E(t) = \frac{1}{2}\sum_{n=1}^{3} E_n(t-t_n)e^{i[\omega_n(t-t_n)-\phi_n]} + \text{c.c.}, \qquad (1)$$

with the Gaussian envelope function $E_n(t-t_n) = A_0/\sigma \exp[-(t-t_n)^2/2\sigma^2]$ centered around t_n, the carrier frequencies ω_n, and the phases ϕ_n, see also Fig. 1(a). For a heterodyne detection scheme, a local oscillator pulse is added in addition to the fields in Eq. (1), allowing us to separate real and imaginary parts of the signal.[41] The incoming pulse train interacts with the sample with a signal phase

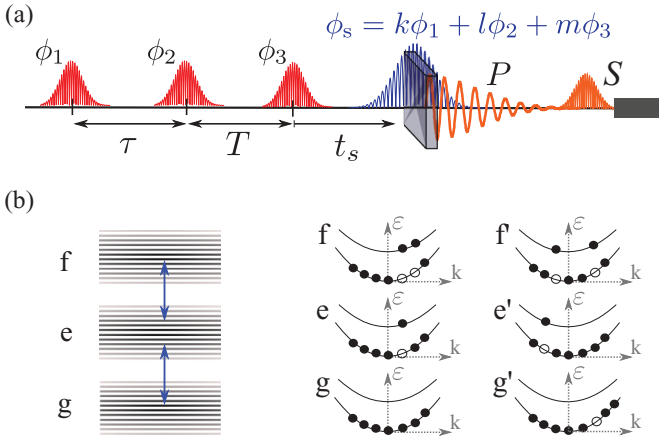

FIG. 1. (Color online) (a) Incoming pulse sequence: The resulting polarization P contains multiple orders in the electron-electromagnetic field interaction. (b) Left: Schematic band diagram of the many-particle state in the χ_3 limit: ground state g, first excited state e, double excited state f. The arrows show the allowed dipole transitions between the states. Right: Two possible electron distributions for the respective many-particle states g/g′, e/e′, f/f′.

$\phi_s = k\phi_1 + l\phi_2 + m\phi_3, \{k,l,m\} \in Z$, representing all possible phase combinations due to nonlinear wave mixing. Thus, the resulting material response of the sample, the macroscopic polarization P (derived in Sec. III) contains multiple sets of Liouville pathways, representing different interactions of the sample with the three incoming pulses which can be classified by the corresponding phase combination. Details are given in the next section. The nonlinear polarization radiates a signal field S which can be detected by either phase sensitive (heterodyne) or phase insensitive (homodyne) schemes. The electric field [Eq. (1)] (and therefore the resulting signal) can be described as a function with respect to the different delay times between the pulses: $E(t) \rightarrow E(\tau,T,t_s)$, with $\tau = t_2 - t_1$, $T = t_3 - t_2$, $t_s = \tau_s - t_3$ as shown in Fig. 1(a).[39,42] For instance, in the heterodyne detection scheme the signal S is given by[38]

$$S(\tau,T,t_s) = \int_{-\infty}^{\infty} dt\, P(t) E^*_{\mathrm{loc}}(t-\tau_s) e^{i\omega_s(t-\tau_s)}, \qquad (2)$$

with the local oscillator field envelope E_{loc} at the signal time τ_s and with the frequency ω_s of the fourth applied pulse to detect the emitted nonlinear polarization $P(t)$. The 2D spectrum is then obtained by Fourier transforming S with respect to the delay times τ and t_s but fixed T, contained in the nonlinear polarization $P(t)$.

For our purpose, the signal phase of interest is the third-order photon echo signal $\Phi_I = -\phi_1 + \phi_2 + \phi_3$ since it allows us to track relaxation processes.[38] Restricting our investigations to the χ_3 response, the electrons in the system are limited to three possible sets of many-particle states with the field: No excitation of the system ground states (g), single excitation (e), and double excitation (f) of the many particle system, all cases shown in Fig. 1(b). For the investigated two-band ISB system, the corresponding subband states are depicted on the right.

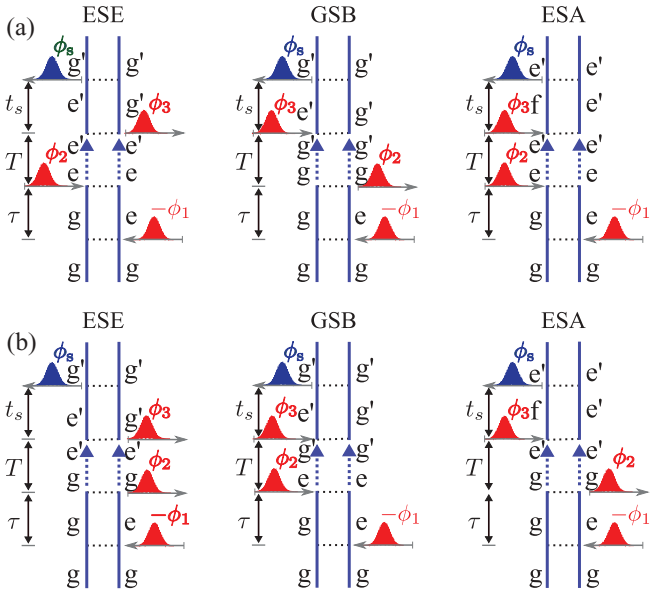

FIG. 2. (Color online) Relevant double-sided Feynman diagrams for the photon echo signal: (a) Intrasubband and (b) intersubband processes for ESE (excited state emission), GSB (ground state bleaching), and ESA (excited state absorption). The dotted arrows represent the temporal evolution of the densities due to relaxation processes.

The physical processes contributing to the Φ_I signal can be interpreted with the relevant double-sided Feynman diagrams[38] of the corresponding Liouville pathways, see Fig. 2. The ket and the bra of the corresponding density matrix are represented by vertical lines (left for ket, right for bra), where, after each time interval, one pulse creates a new state, see Fig. 2. The time evolution goes from bottom to top. An arrow pointing towards the vertical lines symbolizes the transition to a higher excited state and vice versa. If the arrow points to the right, the field comes in with the positive phase, while pointing to the left indicates the interaction with a negative phase. $|g\rangle\langle g|$ and $|g\rangle\langle g'|$ describe the density distribution in the ground state, $|e\rangle\langle e|$ and $|e'\rangle\langle e'|$ is the density distribution in the first excited state. $|g^{(\prime)}\rangle\langle e^{(\prime)}|$, $|e^{(\prime)}\rangle\langle g^{(\prime)}|$ ($|f\rangle\langle e'|$) characterize the coherence between the ground and excited state (first and second excited state). The physical processes at each time can be constructed with the help of double-sided Feynman diagrams. A detailed description for the interpretation of double-sided Feynman diagrams is given in Ref. 38.

For the investigated system we assume spatial homogeneity. Here ISB coherence terms in the form of $|g\rangle\langle g'|$ and $|e\rangle\langle e'|$, which correspond to the coupling of the bra and the ket with different momenta ($\langle a^\dagger_{i,\mathbf{k}} a_{i,\mathbf{k}'}\rangle$), vanish.[43] Under this assumption, six main resonant Liouville pathways remain as contributions to the photon echo signal, which are depicted in Fig. 2, including in the upper panel (a) intrasubband and in the lower panel (b) intersubband relaxation during the waiting time T. The possible intersubband relaxation corresponding to a double excited state absorption, that is, relaxation from $|e\rangle\langle e|$ to $|f\rangle\langle f|$ during T is unlikely and hence not depicted. As an explicit example, the excited state emission (ESE) process for intrasubband relaxation will be interpreted [Fig. 2(a)]: The first

pulse with phase $-\phi_1$ comes in and excites the ground state $|g\rangle\langle g|$ of the system to $|g\rangle\langle e|$. Subsequently, this coherence is destroyed after the delay time τ, where the second pulse with ϕ_2 creates a population $|e\rangle\langle e|$ in the excited state. This population relaxes during the waiting time T, changing to $|e'\rangle\langle e'|$. The third pulse with ϕ_3 again creates a coherence $|e'\rangle\langle g'|$ after t_s. By Fourier transforming with respect to the first (τ) and the third coherence time (t_s), the frequency dependent correlations between the two time delays as a function of the waiting time T can be monitored. As the detected signal field is proportional to the macroscopic polarization in Fourier space[28] [i.e., $S(\omega_\tau,T,\omega_{t_s}) \propto P(\omega_\tau,T,\omega_{t_s})$], we will now introduce the process for the extraction of the specific quantum pathways inherent to the Φ_I signal from P. Since P is uniquely dependent on the phases of the incoming pulses, the selection can be done by a series of experiments, each time with different phases for the pulse sequence. This so called PC technique will be explained in the next section.

II. PHASE CYCLING

As stated in the previous section, the sample can interact multiple times with the three separate pulses of the electric field, each pulse marked by its phase ϕ_i. Each combination of interaction with the field, visible in the signal phase ϕ_s [see Fig. 1(a)], reflects different combinations of quantum pathways. To select the specific Φ_I signal, that is, the case where $-k = l = m = 1$ for ϕ_s, the material response must be decomposed. The nonlinear polarization $P(\tilde{t})$ ($\tilde{t} := \tau,T,t_s$) can be written as a superposition of all directional polarizations $P_{k,l,m}(\tilde{t})$ of these different quantum pathway blocks:[44]

$$P(\tilde{t},\phi_1,\phi_2,\phi_3) = \sum_{k,l,m} P_{k,l,m}(\tilde{t}) e^{i(k\phi_1+l\phi_2+m\phi_3)} + \text{c.c.} = \mathcal{P}(\tilde{t},\phi_1,\phi_2,\phi_3) + \mathcal{P}^*(\tilde{t},\phi_1,\phi_2,\phi_3), \quad (3)$$

with the particular phases of ϕ_i originating from the exciting three pulse sequence. The indices k,l,m indicate the least order of interaction with the respective pulses E_n [Eq. (1)]. For noncollinear pulse propagation, the different $P_{k,l,m}(\tilde{t})$ can be selected by phase matching in different spatial directions. This is not possible for a collinear setup since the pulses are propagating in the same direction. Here, to extract specific directional polarizations one has to repeat the experiment N times, where N is the number of possible combinations of k,l,m. For each experiment the excitation is accompanied by a different set of phase combinations $\Phi_s = (\phi_{1s},\phi_{2s},\phi_{3s})$, where the first index of ϕ_{ns} indicates the phase of the pulse E_n and the second index corresponds to the sth experiment. Using the abbreviation $c_{s,u} = e^{i\mathbf{\Phi}_s\cdot\mathbf{u}}$ with the interaction order $\mathbf{u}$ of the three incoming pulses $\mathbf{u} = (k,l,m)^T$ and $\mathbf{\Phi}_s = \Phi_s^T$, we can rewrite Eq. (3) into a matrix form[44]:

$$\begin{pmatrix} c_{1,1} & c_{1,2} & \dots & c_{1,N} \\ c_{2,1} & c_{2,2} & \dots & c_{2,N} \\ \vdots & \vdots & \ddots & \vdots \\ c_{N,1} & c_{N,2} & \dots & c_{N,N} \end{pmatrix} \begin{pmatrix} P_{\{1\}}(\tilde{t}) \\ P_{\{2\}}(\tilde{t}) \\ \cdots \\ P_{\{N\}}(\tilde{t}) \end{pmatrix} = \begin{pmatrix} \mathcal{P}(\tilde{t},\Phi_1) \\ \mathcal{P}(\tilde{t},\Phi_2) \\ \cdots \\ \mathcal{P}(\tilde{t},\Phi_N) \end{pmatrix}, \quad (4)$$

where $P_{\{u\}} = P_{k,l,m}$. The combination of phases Φ_s can be chosen arbitrarily. Still, the values for ϕ_{1s}, ϕ_{2s}, and ϕ_{3s} should be chosen in order to make $c_{s,u}$ invertible. Corresponding to the number of experiments, N sets of phase combinations are needed. A nonzero determinant of the matrix in Eq. (4) is the only prerequisite for the phase combinations. Inverting this matrix gives the desired directional polarization as a linear combination of the phase-dependent total polarizations $P_{k,l,m}(\tilde{t}) = \sum_{i=1}^{N} c_i^* \mathcal{P}(\tilde{t},\Phi_i)$.

TABLE I. One possible choice for the set of phase combinations of the exciting field (to be multiplied by π).

s	1	2	3	4	5	6	7	8	9	10	11
ϕ_{1s}	0	0	0.5	0.5	1	1	1.5	0	0	0.5	1.5
ϕ_{2s}	0	0	0	0	0	0	0	0	0	0	0
ϕ_{3s}	0	0.5	1	0.5	0	0.5	1.5	1.5	1	1.5	1
s	12	13	14	15	16	17	18	19	20	21	22
ϕ_{1s}	1.5	0	0	0.5	1	1	1.5	0	0	0.5	1.5
ϕ_{2s}	0	1.5	0.5	0.5	0.5	0.5	0.5	0.5	0.5	0.5	0.5
ϕ_{3s}	0.5	0	0.5	1	0	0.5	1.5	1.5	1	1.5	1

The number of possible combinations N is limited by the respective order of the excitation fields E_n. Within this paper the response is restricted to the third-order interaction with the sample. Due to the dipole selection rules of our system, even-order interactions vanish. Thus, 22 possible combinations remain:[39]

$$\begin{aligned} &(\phi_1),(\phi_2),(\phi_3),(3\phi_1),(3\phi_2),(3\phi_3),\\ &(2\phi_1-\phi_2),(2\phi_1-\phi_3),(2\phi_2-\phi_1),\\ &(2\phi_2-\phi_3),(2\phi_3-\phi_1),(2\phi_3-\phi_2),\\ &(2\phi_1+\phi_2),(2\phi_1+\phi_3),(2\phi_2+\phi_1),\\ &(2\phi_2+\phi_3),(2\phi_3+\phi_1),(2\phi_3+\phi_2),\\ &(\phi_1+\phi_2-\phi_3),(\phi_1-\phi_2+\phi_3),(-\phi_1+\phi_2+\phi_3),\\ &(\phi_1+\phi_2+\phi_3). \end{aligned} \quad (5)$$

Accordingly, 22 sets of phase combinations are needed. One possible choice, which has been used for our calculations, is presented in Table I. Since we are interested in the photon echo Φ_I signal, that is, the corresponding directional polarization $P_{-1,1,1}(\tilde{t})$, the phase combinations in Table I were chosen in that manner that only 12 PC steps remain for the extraction of the Φ_I signal $P_{-1,1,1}(\tilde{t})$.

To demonstrate this technique, the 2D spectroscopy with PC is applied to a QW model system. The material response $P(\tilde{t})$ to the exciting pulse sequence arises from the ISB dynamics of the QW. Here the macroscopic polarization is a superposition of the respective dipole transition matrix elements d_{ij} with the microscopic polarizations $\rho_{ij,\mathbf{k}}$. In order to analyze the ISB el-ph quantum kinetics, the model system is described microscopically in the following section.

III. MICROSCOPIC QW MODEL

We investigate an n-doped $GaAs/Al_{0.35}Ga_{0.65}As$ single QW where the dynamics of the lowest two conduction subbands is considered. Nonparabolicity effects are included

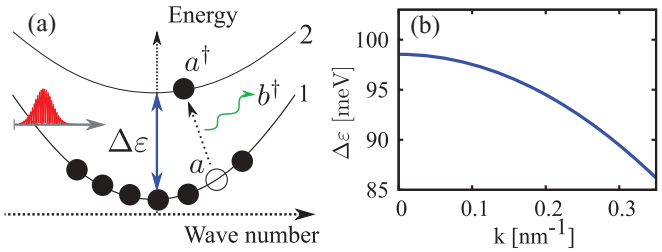

FIG. 3. (Color online) (a) Sketch of the model system showing the transition of an electron from the lower to the upper subband under emission of one phonon. (b) Transition energy $\Delta\varepsilon$ between the two subbands. The energy is decreasing for higher momentum state.

via different effective subband masses m_i.[45] A sketch of the in-plane band structure is given in Fig. 3(a). In our discussion we focus on the coupling of the electrons with a bath of LO bulk phonons. This is a reasonable assumption since the competing el-el interaction is weak for low doping electron densities.[14] Thus, the Hamiltonian of the system consists of the noninteracting 2D confined electrons and bulk phonons ($H_{0,\mathrm{el,ph}}$), the el-LO phonon interaction ($H_{\mathrm{el\text{-}ph}}$), and the electron-electromagnetic (em) field dipole coupling (H_{em}):

$$H_{0,\mathrm{el,ph}} = \sum_{i,\mathbf{k}} \varepsilon_{i,\mathbf{k}} a^\dagger_{i,\mathbf{k}} a_{i,\mathbf{k}} + \sum_{\mathbf{q}} \hbar\omega_{\mathrm{LO}} b^\dagger_{\mathbf{q}} b_{\mathbf{q}}, \tag{6}$$

$$H_{\mathrm{el\text{-}ph}} = \sum_{\mathbf{q},\mathbf{k}} \left(g^{ij}_{\mathbf{q}} a^\dagger_{i,\mathbf{k}} b_{\mathbf{q}} a_{j,\mathbf{k}-\mathbf{q}_\parallel} + g^{ij*}_{\mathbf{q}} a^\dagger_{j,\mathbf{k}-\mathbf{q}_\parallel} b^\dagger_{\mathbf{q}} a_{i,\mathbf{k}} \right), \tag{7}$$

$$H_{\mathrm{em}} = -\sum_{i,j,\mathbf{k}} d_{ij} E(t) a^\dagger_{i,\mathbf{k}} a_{j,\mathbf{k}}, \tag{8}$$

where $a^\dagger_{i\mathbf{k}}$ ($a_{i\mathbf{k}}$) is the creation (annihilation) operator of an electron with an in-plane 2D wave vector $\mathbf{k}$ in subband i and energy $\varepsilon_{i,\mathbf{k}} = \varepsilon_{i,0} + (\hbar^2\mathrm{k}^2/2m_i)$, with the subband energies at the Γ point $\varepsilon_{i,0}$. The different ISB subband masses m_i lead to decreasing transition energies between the subbands $\varepsilon_{2,\mathbf{k}} - \varepsilon_{1,\mathbf{k}} = \Delta\varepsilon_{\mathbf{k}}$ for increasing wave numbers, see Fig 3(b), which will be an important feature for the interpretation of the 2D spectra. $b^\dagger_{\mathbf{q}}$ ($b_{\mathbf{q}}$) labels the creation (annihilation) operator of an LO phonon with the three-dimensional wave vector $\mathbf{q}$ and energy $\hbar\omega_{\mathrm{LO}}$. The in-plane projection of $\mathbf{q}$ is denoted as $\mathbf{q}_\parallel$. Furthermore, $g^{ij}_{\mathbf{q}}$ ($g^{ji*}_{\mathbf{q}}$) is the Fröhlich coupling matrix element[46] which describes the transition of an electron from band j to band i under absorption (emission) of an LO phonon. The semiclassical interaction of the system with an external electromagnetic field $E(t)$ is determined by the dipole matrix element d_{ij}.

The polarization $P(t)$ is the source of the signal detected within this spectroscopy scheme and is calculated from the microscopic polarizations $\rho_{ij,\mathbf{k}}$: $P = 1/A \sum_{ij,\mathbf{k}} d_{ij}\rho_{ij,\mathbf{k}}$ ($i \neq j$).[47] The dynamics for the microscopic polarization $\rho_{ij,\mathbf{k}} = \langle a^\dagger_{i,\mathbf{k}} a_{j,\mathbf{k}} \rangle$, $i \neq j$ and the occupation densities $\rho_{ii,\mathbf{k}} = \langle a^\dagger_{i,\mathbf{k}} a_{i,\mathbf{k}} \rangle$ is calculated within the density matrix formalism using the Heisenberg equation of motion.[48,49] Spatial inhomogeneities are not excited (i.e., $k = k'$). The overall equations, which determine $P(t)$, read[50]

$$\begin{aligned}\dot\rho_{ij,\mathbf{k}} = {} & i\omega_{ij,\mathbf{k}}\rho_{ij,\mathbf{k}} - \frac{iE(t)}{\hbar}\sum_m (d_{mi}\rho_{mj,\mathbf{k}} - d_{jm}\rho_{im,\mathbf{k}}) \\ & + \frac{i}{\hbar}\sum_{o,\mathbf{q}} \left(g^{oi}_{\mathbf{q}} \sigma^{oj}_{\mathbf{k}+\mathbf{q}_\parallel,\mathbf{q},\mathbf{k}} + g^{io*}_{\mathbf{q}} \sigma^{jo*}_{\mathbf{k},\mathbf{q},\mathbf{k}-\mathbf{q}_\parallel} \right. \\ & \left. - g^{jo}_{\mathbf{q}} \sigma^{io}_{\mathbf{k},\mathbf{q},\mathbf{k}-\mathbf{q}_\parallel} - g^{oj*}_{\mathbf{q}} \sigma^{oi*}_{\mathbf{k}+\mathbf{q}_\parallel,\mathbf{q},\mathbf{k}} \right),\end{aligned} \tag{9}$$

with the transition frequency $\omega_{ij,\mathbf{k}} = (\varepsilon_{i,\mathbf{k}} - \varepsilon_{j,\mathbf{k}})/\hbar$ and the phonon-assisted density matrix elements (PADs) $\sigma^{ij}_{\mathbf{k}',\mathbf{q},\mathbf{k}} = \langle a^\dagger_{i,\mathbf{k}'} b_{\mathbf{q}} a_{j,\mathbf{k}} \rangle$. The dynamics of coherent phonons ($\langle b^\dagger \rangle, \langle b \rangle$) is neglected since their contribution is much smaller compared to the dynamics of the PADs.[51] To truncate the system, a second-order Born approximation in $g^{ij}_{\mathbf{q}}$ is applied,[52] where correlated quantities like $\langle a^\dagger a b^\dagger b \rangle$ decouple into phononic and electronic expectation values. This leads to the following equation for the PADs:

$$\begin{aligned}-i\hbar\dot\sigma^{ij}_{\mathbf{k}',\mathbf{q},\mathbf{k}} = {} & (\varepsilon_{i,\mathbf{k}'} - \varepsilon_{j,\mathbf{k}} - \hbar\omega_{\mathrm{LO}})\sigma^{ij}_{\mathbf{k}',\mathbf{q},\mathbf{k}} \\ & - \sum_{mo} g^{mo*}_{\mathbf{q}} [(1+n_{\mathbf{q}})(\delta_{oj} - \rho_{oj,\mathbf{k}})\rho_{im,\mathbf{k}'} \\ & - n_{\mathbf{q}}(\delta_{im} - \rho_{im,\mathbf{k}'})\rho_{oj,\mathbf{k}}] + i\hbar\gamma_{\mathrm{ph}}\sigma^{ij}_{\mathbf{k}',\mathbf{q},\mathbf{k}},\end{aligned} \tag{10}$$

where the occupation of phonon mode $\mathbf{q}$, $n_{\mathbf{q}} = \langle b^\dagger_{\mathbf{q}} b_{\mathbf{q}} \rangle$, is given by the Bose-Einstein distribution function, that is, the bulk phonons are treated as a bath.[50] The occurring four-particle electron operators in the PAD's like $\langle a^\dagger a^\dagger a a \rangle$ are decoupled into electronic expectation values via $\langle a^\dagger_i a^\dagger_j a_m a_n \rangle = \langle a^\dagger_i a_n \rangle \langle a^\dagger_j a_m \rangle - \langle a^\dagger_i a_m \rangle \langle a^\dagger_j a_n \rangle$. Higher order correlations[53] are included as a phenomenological dephasing constant γ_{ph}.[54]

To briefly recap the previous sections: A sequence of pulses $E(t)$ is applied to the introduced microscopic ISB model, which responses with a macroscopic polarization P. This polarization emits a coherent signal arising from a superposition of all possible quantum pathways. To extract the desired pathways, for example, the photon echo signal Φ_I, we use the PC technique. The resulting dynamics are presented in the following section.

IV. RESULTS

A. Absorption and population dynamics

The calculation for the ISB dynamics is done for a 10 nm GaAs/$Al_{0.35}Ga_{0.65}$As quantum well with a gap energy of $\varepsilon_{\mathrm{gap}} = \varepsilon_{2,\mathbf{k}=0} - \varepsilon_{1,\mathbf{k}=0} = 98.54$ meV using a bath temperature of $T = 100$ K.[55] The initial population is assumed to be in thermal equilibrium and occupying the lower subband while the upper subband is empty. In order to interpret the 2D spectra, it is useful to study the underlying ISB processes via the conventional absorption spectra and under different excitation pulses, first.

In the linear regime, the most prominent feature of ISB transitions is already visible in the absorption spectrum, see Fig. 4. Similar to the 2D free carrier spectra in the following subsection, the absorption spectrum is calculated for free electrons, obeying the Pauli principle, with a phenomenological dephasing, that is, the electron-phonon coupling in Eq. (9)

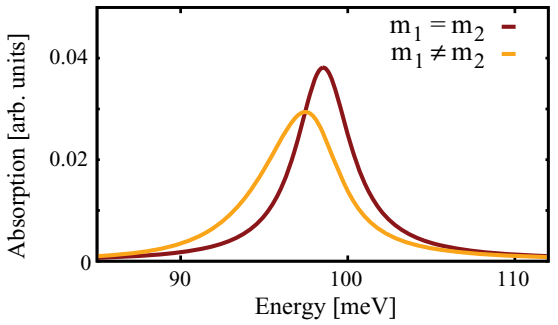

FIG. 4. (Color online) Absorption spectrum for a 10 nm ISB QW for equal subband masses (dark line) and for different subband masses (light line). The spectrum including different subband masses is asymmetrically broadened (low energy tail).

is set to zero. Instead, a dephasing term $-\hbar\gamma\rho_{ij,\mathbf{k}}$ is added to Eq. (9) for the calculation of the microscopic polarization with $\hbar\gamma = 1$ meV for $i \neq j$. Thus, the system is reduced to a set of uncoupled two-level systems with fermionic statistics and has in this case an inherent nonlinearity which is in contrast to the case of an anharmonic oscillator. The spectrum is plotted for equal subband masses (dark line) and different subband masses (light line). For equal subband masses the spectrum has a symmetric line shape around the gap energy ε_{gap}, similar to a homogeneously broadened two-level system. When considering different subband masses, the maximum of the spectrum is shifted to lower energies, combined with a low energy tail. This reflects the density of states as well as the band dispersion since the transition energy $\Delta\varepsilon$ decreases for higher wave numbers $\mathbf{k}$, see also Fig. 3.

Under stronger excitation, nonlinear effects such as nonequilibrium electron occupation and their subsequent relaxation due to el-LO phonon interaction take place. As later used for the 2D spectra, we study the situation where the sample is excited with three Gaussian shaped 0.1π pulses with a standard deviation of $\sigma = 20$ fs, which relates to a FWHM of $\approx$77 meV in the frequency domain. Their frequency is centered around the ISB QW band gap ω_{gap}. In Fig. 5 we analyze the resulting population dynamics. Here, only the first two pulses are applied, separated by a delay time of $\tau = 0.1$ ps. We plot the angle-integrated population distribution for different waiting times T after the second pulse. This situation corresponds to one specific delay time tracked in the photon echo experiment by the third pulse. The upper plot in Fig. 5(a) shows the population distribution of the upper subband $\rho_{22,\text{k}}$. The lower plot displays the change of the population distribution in the lower subband $\rho_{11,\text{k}}$, compared to the distribution before pulse excitation $\rho^0_{11,\text{k}}$: $\rho_{11,\text{k}} - \rho^0_{11,\text{k}}$. In both graphs two x-axis labels are given: The energy (k_i) of the subband i and the corresponding momentum k_i in subband i with energy (k_i) $= \hbar^2\text{k}^2/2m_i$.

Comparing the different waiting times, the electron distribution in the upper subband $\rho_{22,\text{k}}$ decreases for increasing waiting times. This is due to relaxation out of the initially excited nonequilibrium distribution, caused by the exciting pulses with a mean frequency ω_L at the subband gap frequency. The main process is ISB relaxation, which leads to a decrease of $\rho_{22,\text{k}}$ via transfer of electrons with small momentum numbers to the lower subband. The dominant relaxation

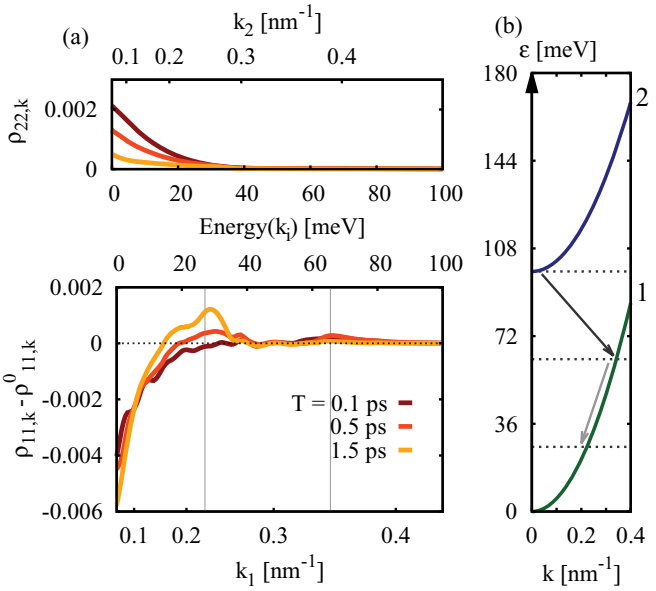

FIG. 5. (Color online) (a) Population distribution of the upper subband $\rho_{22,\mathbf{k}}$ (upper panel) and differential population distribution of the lower subband $\rho_{11,\mathbf{k}} - \rho^0_{11,\mathbf{k}}$ (lower panel) for three different waiting times T. $\rho^0_{11,\mathbf{k}}$ is the population distribution in the lower subband before the excitation with the pulses. The delay time τ is set to 0.1 ps. The distributions are plotted after excitation with the first two pulses. (b) Band dispersion of the lower subband 1 and the upper subband 2. The gray arrows mark the electron relaxation processes from the upper subband minimum under emission of one LO phonon. The dotted lines are spaced with a distance of one LO phonon energy $\hbar\omega_{\text{LO}} = 36$ meV.

channel is pictured in Fig. 5(b), where the energy dispersion of the subbands is displayed: First, the excited electrons relax from the upper subband minimum to the lower subband at $\text{k} \approx 0.35\,\text{nm}^{-1}$ [dark arrow in Fig. 5(b)], due to approximate energy conservation (one LO phonon energy). This leads to the slightly increased occupation $\rho_{11,\text{k}}$ with $\text{k} \approx 0.35\,\text{nm}^{-1}$ in Fig. 5(a) for $T = 0.5$ ps. Then, electrons can further relax within the lower subband to around $\text{k} \approx 0.22\,\text{nm}^{-1}$. These processes take place under emission of one LO phonon with an approximate energy transfer of $\varepsilon_{\text{LO}} = 36$ meV, indicated in Fig. 5(b) as horizontal dotted lines. Since the momentum state $\text{k} \approx 0.22\,\text{nm}^{-1}$ is less than one LO phonon energy above the lower subband minimum, the distribution $\rho_{11,\text{k}\approx 0.22\,\text{nm}^{-1}}$ increases for higher waiting times T, see also the lower graph in Fig. 5(a). Under excitation with more spectrally sharp pulses, these phonon replica would be more pronounced, similar to observations in intraband systems.[53,56] In our case the replica are broadened due to the large spectral pulses.

Next, the 2D photon echo signal will be investigated. For comparison, we start the analysis with the spectrum for the free carrier dynamics (Sec. IV B). Subsequently, the el-LO phonon interaction is included and their effects onto the 2D spectrum will be discussed for different waiting times T (Sec. IV C). The $\Phi_I = -\phi_1 + \phi_2 + \phi_3$ signal $P_{-1,1,1}(\tau, T, t_s)$ is extracted with the 12-step PC protocol explained in Sec. II. By Fourier transforming with respect to τ and t_s, the 2D photon echo signal $P_{-1,1,1}(\hbar\omega_\tau, T, \hbar\omega_{t_s})$ is obtained.

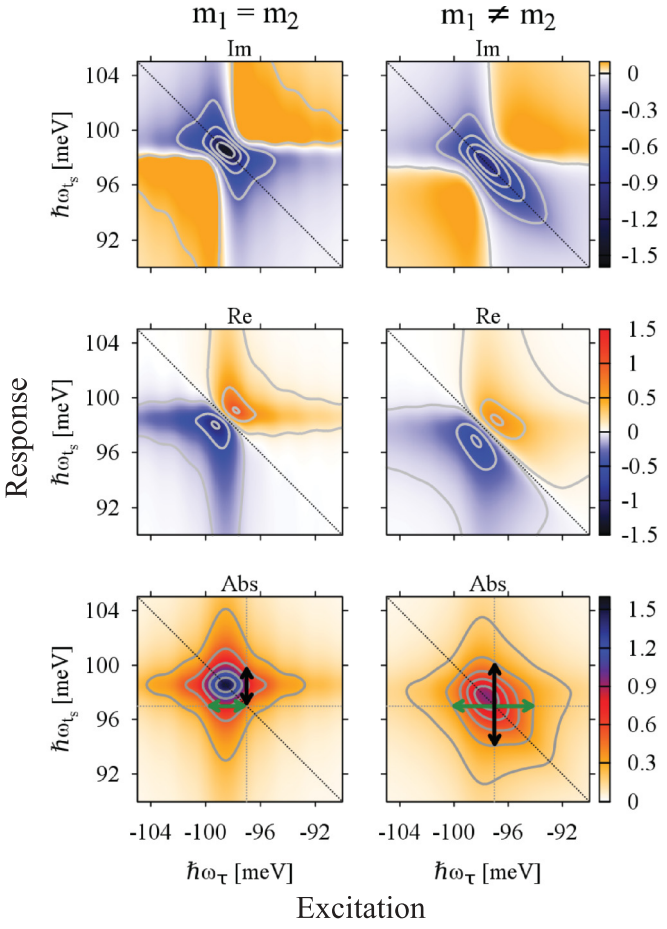

FIG. 6. (Color online) 2D free carrier spectra of the photon echo signal $P_{-1,1,1}$ in a 10 nm ISB QW including equal subband masses (left column) and different subband masses (right column) for $T = 0.5$ ps. From top to bottom are shown the imaginary, real, and absolute parts of the signal. The contour lines of the absolute parts are equally spaced with a distance of 1/6 of the maximum strength.

B. 2D free carrier spectra

Figure 6 shows $P_{-1,1,1}(\hbar\omega_\tau, T, \hbar\omega_{t_s})$ for a free carrier system with equal (left column) and different subband masses (right column). Their imaginary, real, and absolute parts are shown from top to bottom. The color bar determines the signal strength over the energies $\hbar\omega_\tau$ along the horizontal axis and $\hbar\omega_{t_s}$ along the vertical axis. In terms of the Φ_I signal, ω_τ is called excitation frequency since τ is the time after the first pulse exciting the initial population. The signal time t_s after the third pulse provides information about the development of the excited system, hence ω_{t_s} is denoted as response frequency. Thus, the 2D spectra present a mapping of excitation and response. In standard photon echo spectra,[57] only the signal along one frequency axis is resolved. In the case of 2D spectroscopy, more detailed information can be gained by comparing excitation and response frequencies. This allows us to study the development of the population through the correlation of excitation and response frequencies during fixed waiting times T: If the population remains unchanged during T, the spectrum shows a diamond-shaped symmetry along the $-\hbar\omega_\tau = \hbar\omega_{t_s}$ axis since the excitation and response populations do not alter. Population changes on the other hand are visible as asymmetries in the spectra. The different signs of these two axes originate from the opposing phases of the first and the third exciting pulse.

The free carrier spectrum with equal subband masses exhibits strong symmetries: The real and imaginary spectra are symmetric along and perpendicular to the diagonal. Hence, the absolute, diamond-shaped signal (Fig. 6 bottom left) has diagonal and antidiagonal symmetry as known from 2D spectra of a two-level system.[58] For different subband masses (Fig. 6, right column), the imaginary and real spectra become asymmetric along the antidiagonal and the spectrum is stretched towards lower energies along the diagonal. Also, the maximum of the signal is shifted to lower energies. Still, since no population relaxation occurs, the signal is symmetric along the diagonal. The signal along $-\hbar\omega_\tau = \hbar\omega_{t_s}$ reflects the density of states for different subband masses as explained in Fig. 4 and leads to a slender elongation along the dotted diagonal: The width of the signal along $\hbar\omega_{t_s} = \text{const}$ is determined by the homogeneous linewidth due to photon echo, while the width along $-\hbar\omega_\tau = \hbar\omega_{t_s}$ is inhomogeneously broadened by the possible transition energies made available by the electron occupation.[59] Therefore, since every transition energy can be assigned to one specific wave number, the Φ_I signal enables the sampling of the subbands.

The underlying physical process causing the symmetric shape of the free carrier spectra is best understood in terms of the double-sided Feynman diagrams, Fig. 2: Lacking many-particle interactions in the free carrier spectrum, the density distributions $|g\rangle\langle g|$ and $|e\rangle\langle e|$ do not alter during any waiting time T, which is equivalent to sampling the same available transition energies after the first and the third pulse. As an example, the occupation probability along $\hbar\omega_\tau = -97$ meV will be compared with the one at $\hbar\omega_{t_s} = 97$ meV at the contour of 1/3 of the signal strength, see arrows in Fig. 6 bottom left: In the spectrum including equal subband masses, the response occupation probability along one excitation energy (dark vertical arrow) equals the excitation occupation probability along the appropriate response energy (light horizontal arrow). This is also the case for the free carrier spectrum with different subband masses (arrows in Fig. 6 bottom right). Thus, the 2D spectra give the same information about the occupation probability in the momentum space for the initial population along the $\hbar\omega_{t_s}$ axis as well as for the population after the waiting time T along $\hbar\omega_\tau$.

C. 2D el-ph interaction dominated spectra

In the next step we include the el-LO phonon interaction, Eqs. (9) and (10). Now, when a coherence is created by a pulse, the coupling to the phonon bath will lead to a dephasing and relaxation, which alters the dynamics for different waiting times, as already seen in Fig. 5. The typical time scale of the el-ph interaction is on the scale of $\tau_{\text{int}} \sim 1$ ps.[60] Therefore, we expect typical effects for $T \to \tau_{\text{int}}$. Figure 7, left column, shows the absolute $P_{-1,1,1}$ 2D spectrum including el-LO phonon interaction for three different waiting times of $T = 0.1$, 0.5, and 1.5 ps from top to bottom. To follow the development of the population of the carriers, the response signal is displayed as 1D cuts for three different

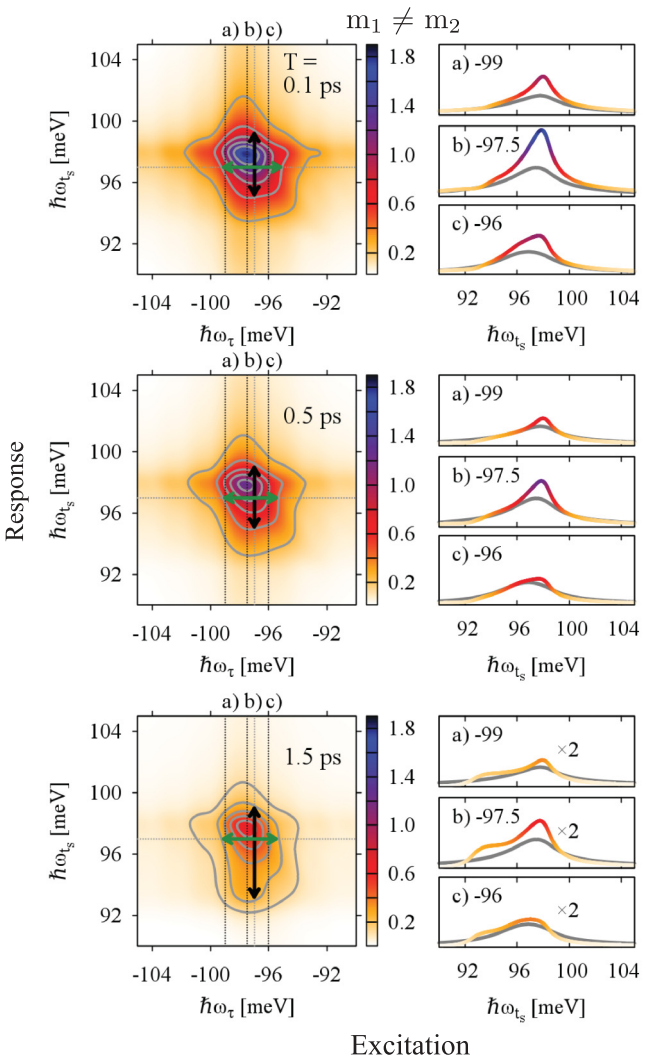

FIG. 7. (Color online) Left column: Absolute 2D photon echo spectra including el-LO phonon interaction for three different waiting times, showing the mapping of excitation and response energy for top: $T = 0.1$ ps, middle: $T = 0.5$ ps, bottom: $T = 1.5$ ps. Right column: Occupation probability (colored cuts) of the response energy for three different excitation energies (along the dotted lines in the 2D spectra). The gray lines in the right column are the appropriate cuts for the noninteracting system. For longer waiting times, electron relaxation takes place, visible as an increasing signal at $\hbar\omega_{t_s} \approx 94$ meV. The contour lines are equally spaced with a distance of 1/6 of the maximum strength.

excitation energies at $\hbar\omega_\tau =$ (a) -99 meV, (b) -97.5 meV, and (c) -96 meV, colored lines in Fig. 7, right column. For comparison we also added the appropriate cuts for the noninteracting system (gray lines), taken from Fig. 6, bottom right. One clearly recognizes that the el-LO phonon interaction induced occupation probability strongly alter for different T. The phases of the refractive (Re) and the absorptive (Im) signal (not shown here) do not change in sign for different T, indicating that relaxation processes related to varying T are phase insensitive. For larger waiting times, the spectrum becomes asymmetric regarding the diagonal, visible as a shift of the signal to lower energies along $\hbar\omega_{t_s}$. This increasing asymmetry is the result of the redistribution of the electrons within and between the subbands due to ISB relaxation, for example, the pathway $|e\rangle\langle e| \rightarrow |g'\rangle\langle g'|$ (the GSB process in the lower panel) and the pathways with the states $|e'\rangle\langle e'|$ at the end of T (ESE and ESA processes in Fig. 2). Since the electron-phonon interaction is responsible for the dephasing, the homogeneous linewidth (along $\hbar\omega_{t_s} = \text{const}$) of the 2D spectra in Fig. 7 is determined by the T_2 time.

For $T = 0.1$ ps (Fig. 7, top left), similar to the free carrier model a low energy tail along the diagonal is visible which is comparable to the free carrier spectrum with different subband masses (Fig. 6, bottom right). This low energy tail is also present at the different response signals for different excitation energies (Fig. 7, top right). Also, the signal is still quite symmetric along the diagonal. This almost symmetric signal shape indicates that the population of the subbands has hardly changed during $T = 0.1$ ps. As in the case of the free carrier dynamics, the first and third pulse sample nearly the same available transition energies, leading to the conclusion that during a waiting time of $T = 0.1$ ps, almost no relaxation occurred.

Comparing the 1D cuts for $T = 0.1$ ps (Fig. 7, top right) and $T = 0.5$ ps (Fig. 7, middle right), a reduction in the signal strength is visible for increasing T. This is a result of the relaxation between subbands with LO phonons of presumably high parallel momentum. A signal reduction for decreasing density in the upper subband occurs since the spectra show the *difference* of the present population to the initial ground state distribution $|g\rangle\langle g|$.[59] For $T = 0.1$ and 0.5 ps the maximum of the 2D signal strength lies around the shifted gap energy with monotonic signal decrease, corresponding to the change of the subband populations $\rho_{22,k}$ and $\rho_{11,k}$ around the subband minima, see the dark lines in Fig. 5(a) in the lower and the upper graph. A slight asymmetry along the diagonal can already be seen in the 2D spectrum for $T = 0.5$ ps since there is a small low energy shift along the response energy $\hbar\omega_{t_s}$ axis. This indicates the beginning of ISB relaxation; the comparison of response and the excitation probability for the respective excitation and response energies does not lead to the same occupation probability (cf. dark and light arrow in Fig. 7, middle). Note, that besides the signal reduction, the line shapes in the 1D cuts do not visibly change for different $T = 0.1$ ps and $T = 0.5$ ps. However, the 2D spectrum for $T = 0.5$ ps already reveals electron relaxation when mapping the excitation and response energy.

For $T = 1.5$ ps, the asymmetry of the 2D spectrum (Fig. 7, bottom left) further increases, exposing a very clear difference between the excitation and response occupation probabilities as denoted with the light and dark arrow. The comparison between the spectra for different T approve that the el-LO phonon scattering time lies in the well-known picosecond range.[60] The 1D cuts for $T = 1.5$ ps (Fig. 7, bottom right) show an increased signal around the energy of $\hbar\omega_{t_s} \approx 94$ meV, suggesting ISB relaxation. Comparing this with the population distributions at $T = 1.5$ ps [light lines in Fig. 5(a)], the increased signal along the response energy $\hbar\omega_{t_s} \approx 94$ meV in Fig. 7, bottom, corresponds to the increased occupation of $\rho_{11,k}$ at $k \approx 0.22\ \text{nm}^{-1}$ in Fig. 5(a). The equivalence is shown in Fig. 3(b), where the transition energy is plotted over the momentum number. Consequently, the 2D spectrum for $T = 1.5$ ps reproduces the dynamics of

the population distributions. As already discussed in Sec. IV A, this increase is due to a two-step electron relaxation from the upper subband minimum to the lower subband. Note that the absolute value of the increased population distribution at $\rho_{11,k\approx 0.22\,nm^{-1}}$ is very small compared to the initial ground state population distribution $\rho^0_{11,k}$. But since the 2D photon echo samples the *difference* between the present distribution and the initial distribution, even small changes in the system can be detected.

Hence, the main feature of the temporal development of the population, namely the electronic ISB relaxation which results in an increased population in the lower subband at $k \approx 0.22\ nm^{-1}$, can be clearly resolved in the 2D photon echo signal. Thus we conclude, that the presented technique is very well suited for the detection of many-body interactions in ISB systems. To summarize: The relaxation of the population can be followed in the Fourier transform 2D spectra for different waiting times by monitoring the excitation and response occupation probabilities over a broad spectral range.

V. CONCLUSIONS

In conclusion, we studied the 2D photon echo signal for a single intersubband quantum well. We simulated a collinear three pulse setup and applied a phase cycling protocol for the extraction of different quantum pathways. The resulting response of the intersubband system was analyzed in the frequency domain for different waiting times. The comparison between the different 2D spectra gives direct information about the development of the occupation probability. While for earlier waiting times the electron distribution has hardly changed, the 2D spectrum for $T = 1.5$ ps shows strong asymmetries along the excitation and response frequency diagonal, which indicates electronic intersubband relaxation due to the electron-phonon coupling. Hereby it is possible to map excitation and response frequencies independently and thus to get accurate information about the dynamics of the electronic occupation probability. The simulations demonstrate that the 2D Fourier spectroscopy is a powerful tool for the detection of many-body correlations and electronic dynamics. Furthermore, the technique is capable of the extraction of other signals, such as the antiphoton echo and double quantum coherence, which will be interesting aspects for further investigations.

ACKNOWLEDGMENTS

We thank F. Milde for fruitful discussions. Financial support by the Deutsche Forschungsgemeinschaft (DFG) through the project KN 427/4-1 (T. U.-K. Dang, C. Weber, and A. Knorr) and by the Sfb 787 (M. Richter) is gratefully acknowledged.

*uyen@itp.tu-berlin.de
†Now at Carl Zeiss AG, Oberkochen, Germany.
‡Now at Technische Universität Wien, Austria.

[1] J. Faist, F. Capasso, D. L. Sivco, C. Sirtori, A. L. Hutchinson, and A. Y. Cho, Science **264**, 553 (1994).
[2] C. Gmachl, F. Capasso, D. L. Sivco, and A. Y. Cho, Rep. Prog. Phys. **64**, 1533 (2001).
[3] C. Weber, A. Wacker, and A. Knorr, Phys. Rev. B **79**, 165322 (2009).
[4] B. Nottelmann, V. Axt, and T. Kuhn, Physica B: Condensed Matter **272**, 234 (1999).
[5] R. A. Kaindl, K. Reimann, M. Woerner, T. Elsaesser, R. Hey, and K. H. Ploog, Phys. Rev. B **63**, 161308 (2001).
[6] J. Li and C. Z. Ning, Phys. Rev. Lett. **91**, 097401 (2003).
[7] I. Waldmüller, J. Förstner, S.-C. Lee, A. Knorr, M. Woerner, K. Reimann, R. A. Kaindl, T. Elsaesser, R. Hey, and K. H. Ploog, Phys. Rev. B **69**, 205307 (2004).
[8] D. Golde, M. Wagner, D. Stehr, H. Schneider, M. Helm, A. M. Andrews, T. Roch, G. Strasser, M. Kira, and S. W. Koch, Phys. Rev. Lett. **102**, 127403 (2009).
[9] M. Vogel, A. Vagov, V. M. Axt, A. Seilmeier, and T. Kuhn, Phys. Rev. B **80**, 155310 (2009).
[10] R. Huber, A. A. Anappara, G. Günter, A. Sell, S. D. Liberato, C. Ciuti, G. Biasiol, L. Sorba, A. Tredicucci, and A. Leitenstorfer, J. Appl. Phys. **109**, 102418 (2011).
[11] I. Waldmüller, M. Woerner, J. Förstner, and A. Knorr, Phys. Status Solidi B **238**, 474 (2003).
[12] S. Butscher and A. Knorr, Phys. Rev. Lett. **97**, 197401 (2006).
[13] T. U.-K. Dang, C. Weber, M. Richter, and A. Knorr, Phys. Rev. B **82**, 045305 (2010).
[14] V. M. Axt and T. Kuhn, Rep. Prog. Phys. **67**, 433 (2004).
[15] N. Iizuka, K. Kaneko, N. Suzuki, T. Asano, S. Noda, and O. Wada, Appl. Phys. Lett. **77**, 648 (2000).
[16] Z. Wang, K. Reimann, M. Woerner, T. Elsaesser, D. Hofstetter, J. Hwang, W. J. Schaff, and L. F. Eastman, Phys. Rev. Lett. **94**, 037403 (2005).
[17] Z. Wang, K. Reimann, M. Woerner, T. Elsaesser, D. Hofstetter, E. Baumann, F. R. Giorgetta, H. Wu, W. J. Schaff, and L. F. Eastman, Appl. Phys. Lett. **89**, 151103 (2006).
[18] R. R. Ernst, G. Bodenhausen, and A. Wokaun, *Principles of Nuclear Magnetic Resonance in One or Two Dimensions* (Clarendon, Oxford, 1998).
[19] A. Wokaun and R. Ernst, Chem. Phys. Lett. **52**, 407 (1977).
[20] D. M. Jonas, Annu. Rev. Phys. Chem. **54**, 425 (2003).
[21] S. A. Diddams, D. J. Jones, J. Ye, S. T. Cundiff, J. L. Hall, J. K. Ranka, R. S. Windeler, R. Holzwarth, T. Udem, and T. W. Hänsch, Phys. Rev. Lett. **84**, 5102 (2000).
[22] C. Brenner, M. Hofmann, M. Scheller, M. K. Shakfa, M. Koch, I. C. Mayorga, A. Klehr, G. Erbert, and G. Tränkle, Opt. Lett. **35**, 3859 (2010).
[23] Y. Tanimura and S. Mukamel, J. Chem. Phys. **99**, 9496 (1993).
[24] I. Kuznetsova, T. Meier, S. T. Cundiff, and P. Thomas, Phys. Rev. B **76**, 153301 (2007).
[25] J. Kim, S. Mukamel, and G. D. Scholes, Acc. Chem. Res. **42**, 1375 (2009).
[26] D. Abramavicius and S. Mukamel, J. Chem. Phys. **133**, 064510 (2010).
[27] S. Mukamel and M. Richter, Phys. Rev. A **83**, 013815 (2011).
[28] T. Brixner, T. Mančal, I. V. Stiopkin, and G. R. Fleming, J. Chem. Phys. **121**, 4221 (2004).

[29]M. Cho, Chem. Rev. **108**, 1331 (2008).
[30]S. T. Cundiff, T. Zhang, A. D. Bristow, D. Karaiskaj, and X. Dai, Acc. Chem. Res. **42**, 1423 (2009).
[31]F. Milota, J. Sperling, A. Nemeth, D. Abramavicius, S. Mukamel, and H. F. Kauffmann, J. Chem. Phys. **131**, 054510 (2009).
[32]I. Kuznetsova, N. Gögh, J. Förstner, T. Meier, S. T. Cundiff, I. Varga, and P. Thomas, Phys. Rev. B **81**, 075307 (2010).
[33]W. Kuehn, K. Reimann, M. Woerner, T. Elsaesser, R. Hey, and U. Schade, Phys. Rev. Lett. **107**, 067401 (2011).
[34]M. Khalil, N. Demirdöven, and A. Tokmakoff, J. Phys. Chem. A **107**, 5258 (2003).
[35]L. Seidner, G. Stock, and W. Domcke, J. Chem. Phys. **103**, 3998 (1995).
[36]B. Wolfseder, L. Seidner, G. Stock, and W. Domcke, Chem. Phys. **217**, 275 (1997).
[37]H.-S. Tan, J. Chem. Phys. **129**, 124501 (2008).
[38]D. Abramavicius, B. Palmieri, D. V. Voronine, F. Sanda, and S. Mukamel, Chem. Rev. **109**, 2350 (2009).
[39]T. Kato and Y. Tanimura, Chem. Phys. Lett. **341**, 329 (2001).
[40]P. Tian, D. Keusters, Y. Suzaki, and W. S. Warren, Science **300**, 1553 (2003).
[41]L. Lepetit, G. Chériaux, and M. Joffre, J. Opt. Soc. Am. B **12**, 2467 (1995).
[42]S. Yan and H.-S. Tan, Chem. Phys. **360**, 110 (2009).
[43]F. Steininger, A. Knorr, T. Stroucken, P. Thomas, and S. W. Koch, Phys. Rev. Lett. **77**, 550 (1996).
[44]S. Meyer and V. Engel, Appl. Phys. B **71**, 293 (2000).
[45]U. Ekenberg, Phys. Rev. B **40**, 7714 (1989).
[46]J. Li and C. Z. Ning, Phys. Rev. B **70**, 125309 (2004).
[47]W. Schäfer and M. Wegener, *Semiconductor Optics and Transport Phenomena* (Springer, Heidelberg, 2002).
[48]H. Haug and S. W. Koch, *Quantum Theory of the Optical and Electronic Properties of Semiconductors* (World Scientific, Singapore, 2004).
[49]E. Malic, C. Weber, M. Richter, V. Atalla, T. Klamroth, P. Saalfrank, S. Reich, and A. Knorr, Phys. Rev. Lett. **106**, 097401 (2011).
[50]S. Butscher, J. Förstner, I. Waldmüller, and A. Knorr, Phys. Rev. B **72**, 045314 (2005).
[51]T. Papenkort, T. Kuhn, and V. M. Axt, Phys. Rev. B **81**, 205320 (2010).
[52]T. Kuhn, in *Theory of Transport Properties of Semiconductor Nanostructures*, edited by E. Schöll (Chapman Hall, London, 1998).
[53]J. Schilp, T. Kuhn, and G. Mahler, Phys. Rev. B **50**, 5435 (1994).
[54]Within our calculations, $\hbar\gamma_{\rm ph} = 1$ meV, which does not affect the optical spectra, see also Ref. 61.
[55]Further parameters were used for our calculations: Effective subband masses $m_1 = 0.0712m_0$, $m_2 = 0.0877m_0$, longitudinal optical phonon energy $\hbar\omega_{\rm LO} = 36$ meV, electron density $n_{\rm dop} = 5 \times 10^{-10}$ cm^{-2}, static dielectric constant $\varepsilon_0 = 12.9$, and high-frequency dielectric constant $\varepsilon_\infty = 10.9$.
[56]R. Zimmermann, J. Wauer, A. Leitenstorfer, and C. Fürst, J. Lumin. **76**, 34 (1998).
[57]S. Mukamel, *Principles of Nonlinear Optical Spectroscopy* (Oxford University Press, New York, 1995).
[58]M. Khalil, N. Demirdöven, and A. Tokmakoff, Phys. Rev. Lett. **90**, 047401 (2003).
[59]S. Mukamel, Annu. Rev. Phys. Chem. **51**, 691 (2000).
[60]S. Rudin and T. L. Reinecke, Phys. Rev. B **41**, 7713 (1990).
[61]S. Butscher, J. Förstner, I. Waldmüller, and A. Knorr, Phys. Status Solidi B **241**, R49 (2004).